Spin-Orbit Coupling for Photons and Polaritons in Microstructures

V. G. Sala,[1,2] D. D. Solnyshkov,[3] I. Carusotto,[4] T. Jacqmin,[1,*] A. Lemaître,[1] H. Terças,[3] A. Nalitov,[3] M. Abbarchi,[1,5,†] E. Galopin,[1] I. Sagnes,[1] J. Bloch,[1] G. Malpuech,[3] and A. Amo[1]

[1]*Laboratoire de Photonique et Nanostructures, LPN/CNRS, Route de Nozay, 91460 Marcoussis, France*
[2]*Laboratoire Kastler Brossel, Université Pierre et Marie Curie, École Normale Supérieure et CNRS, UPMC Case 74, 4 place Jussieu, 75252 Paris Cedex 05, France*
[3]*Institut Pascal, Photon-N2, Clermont Université and Université Blaise Pascal, CNRS, 63177 Aubière Cedex, France*
[4]*INO-CNR BEC Center and Dipartimento di Fisica, Università di Trento, I-38123 Povo, Italy*
[5]*Laboratoire Pierre Aigrain, École Normale Supérieure, CNRS (UMR 8551), Université Pierre et Marie Curie, Université Paris Diderot, 75005 Paris, France*

(Received 23 October 2014; revised manuscript received 20 January 2015; published 25 March 2015)

We use coupled micropillars etched out of a semiconductor microcavity to engineer a spin-orbit Hamiltonian for photons and polaritons in a microstructure. The coupling between the spin and orbital momentum arises from the polarization-dependent confinement and tunneling of photons between adjacent micropillars arranged in the form of a hexagonal photonic molecule. It results in polariton eigenstates with distinct polarization patterns, which are revealed in photoluminescence experiments in the regime of polariton condensation. Thanks to the strong polariton nonlinearities, our system provides a photonic workbench for the quantum simulation of the interplay between interactions and spin-orbit effects, particularly when extended to two-dimensional lattices.

DOI: 10.1103/PhysRevX.5.011034

Subject Areas: Condensed Matter Physics, Photonics, Semiconductor Physics

I. INTRODUCTION

Spin-orbit (SO) coupling is the coupling between the motion and spin of a particle. It gives rise to the fine structure in atomic spectra, and it is naturally present in some bulk materials. Prominent examples are semiconductors without inversion symmetry [1], in which static electric fields in the crystal Lorentz transform to a magnetic field in the reference frame of a moving electron, which then couples to the electron spin. The resulting SO coupling leads to a number of exciting phenomena like the spin-Hall effect [2,3], the persistent spin helix [4], or topological insulation in the absence of any external magnetic field [5].

In semiconductors the SO coupling is determined by the crystalline structure. It is, therefore, hard to manipulate and often difficult to separate from other effects. Novel systems, like ultracold atomic gases under suitably designed optical and/or magnetic field configurations [6], and photons in properly designed structures [7], allow for a great flexibility and control of the system Hamiltonian. Even though particles without a magnetic moment cannot experience the usual SO coupling, the engineering of an effective Hamiltonian acting on photons in structured media has led, for instance, to the observation of the photonic analogue of the spin-Hall effect in planar structures [8,9] and in metasurfaces [10], and unidirectional photon transport in lattices with topological protection from disorder scattering [11–13]. Effective SO couplings have been induced in arrays of photonic ring resonators using the spinlike degree of freedom associated with the rotation direction of photons in the resonator [13,14].

A promising perspective to induce SO coupling in photonic systems is to use the intrinsic photon spin: the polarization degree of freedom [15]. In combination with the strong spin-dependent interactions naturally present in microcavity-polariton devices and the possibility of scaling up to lattices of arbitrary geometry [16–18], the realization of such a coupling in semiconductor microcavities would open the way to the simulation of many-body effects in a new quantum optical context [19]. Some examples would be the controlled nucleation of fractional topological excitations [20,21], the formation of polarization patterns [22,23], the simulation of spin models using photons [24], topological insulation [25,26], or the generation of fractional quantum Hall states for light [27,28].

*Present address: Laboratoire Kastler Brossel, UPMC-Sorbonne Universités, CNRS, ENS-PSL Research University, Collège de France, 4 place Jussieu, Case 74, F75252 Paris Cedex 05, France.

†Present address: CNRS, Aix-Marseille Université, Centrale Marseille, IM2NP, UMR 7334, Campus de St. Jérôme, 13397 Marseille, France.

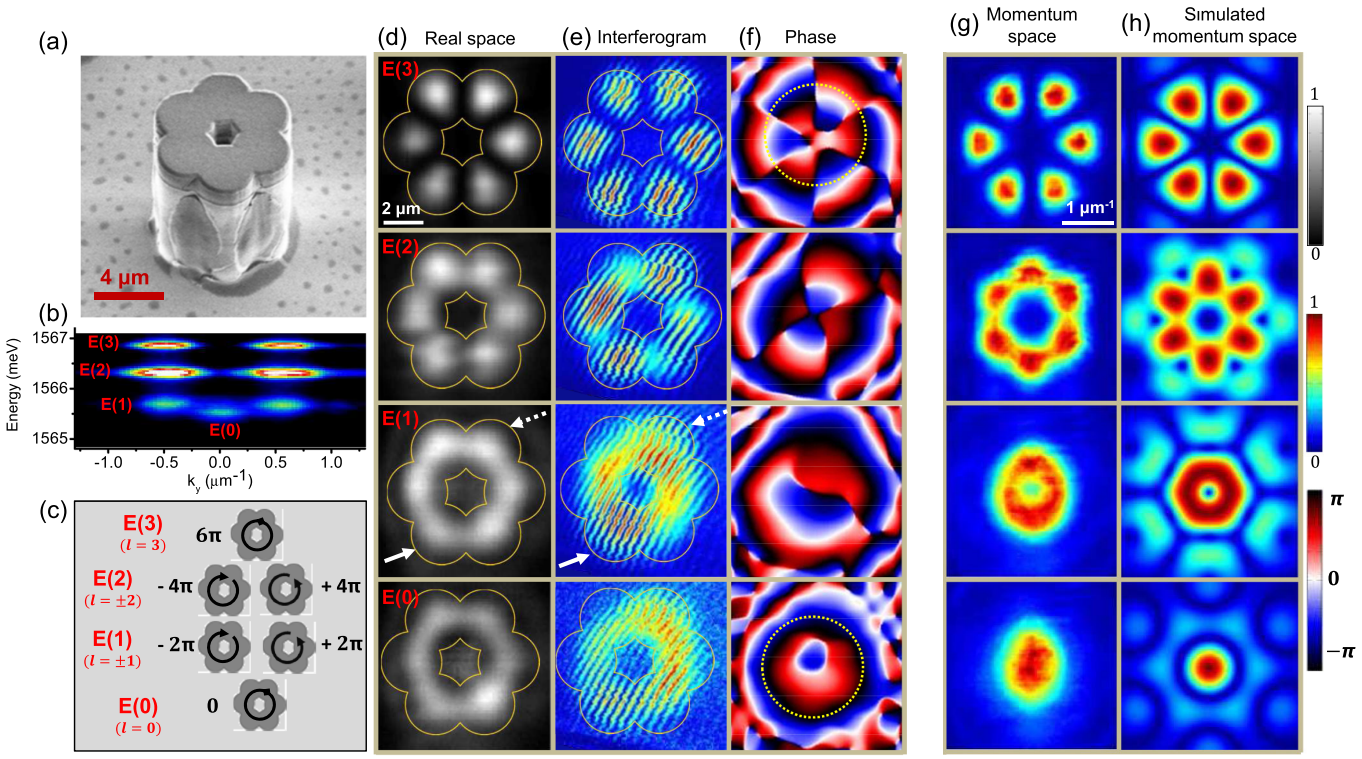

FIG. 1. Photonic molecular states. (a) Scanning electron microscope image of the polaritonic molecule. (b) Polarization-insensitive emission spectrum in momentum space at $k_x = 0.2$ μm and low excitation power (7 mW), showing the four molecular states $E(0), \ldots, E(3)$ arising from the coupling of the lowest energy mode of each single micropillar. (c) Scheme of the phase winding of the eigenfunctions of the $E(l)$ states without accounting for the spin. (d) Measured polarization-insensitive real-space emission. (e) Interference pattern and (f) extracted phase for each of the individual emission lines. The solid arrow points the pillar used for the phase reference in the interference experiment. (g) Measured polarization-insensitive momentum-space emission. (h) Simulated momentum-space emission obtained by Fourier transforming the tight-binding model eigenfunctions with a Gaussian distribution over each lobe.

In this article, we report on the engineering of the coupling between the polarization (spin) and the momentum (orbital) degrees of freedom of polaritons using a photonic microstructure with a ringlike shape. The structure is a hexagonal chain of overlapping micropillars as shown in Fig. 1(a). Each individual micropillar shows discrete confined photonic modes. Thanks to the spatial overlap of adjacent micropillars, the photons can tunnel between neighboring sites [29,30] with an amplitude that is different for the polarization states parallel and orthogonal to the link direction, as recently reported in Ref. [31] [Figs. 2(a) and 2(b)]. We show here that when extended to the hexagonal structure, the polarization-dependent tunneling, together with on-site polarization splittings, results in an effective SO coupling for photons. In our system, photons are strongly coupled to quantum-well excitons, giving rise to polariton states, which hold the same polarization properties of the confined photons. We show that the engineered SO coupling drives the condensation of polaritons into states with complex spin textures.

II. HEXAGONAL PHOTONIC MOLECULE

To evidence experimentally the SO coupling, we use a polaritonic structure fabricated from a planar $Ga_{0.05}Al_{0.95}As$ $\lambda/2$ cavity embedded in $Ga_{0.05}Al_{0.95}As/Ga_{0.8}Al_{0.2}As$ Bragg mirrors with 28 (40) top (bottom) pairs, with a quality factor $Q = 72000$ measured in a resonant excitation experiment. Three sets of four GaAs quantum wells 7 nm in width are epitaxially grown at the central maxima of the electromagnetic field of the structure, resulting in photon-exciton strong coupling with a Rabi splitting of 15 meV [18]. We engineer hexagonal molecules made out of six round micropillars that are etched in the planar microcavity in a region with a detuning between cavity and exciton of −5 meV [Fig. 1(a)]. Each individual micropillar, with a diameter of 3 μm, is a zero-dimensionally-confined photonic box with discrete eigenstates [33]. The one with the lowest energy has s symmetry (cylindrical with a maximum at the center of the pillar) [29]. In our structure, the center-to-center distance between the micropillars is 2.4 μm, smaller than the diameter, resulting in the spatial overlap of adjacent micropillars. The overlap gives rise to a tunneling coupling of polaritons, via their photonic component, between neighboring micropillars, which amounts to 0.3 meV [29,30]. The polarization dependence of the electromagnetic-field penetration out of the edges of the micropillars results in a polarization dependence of the tunneling rate [31].

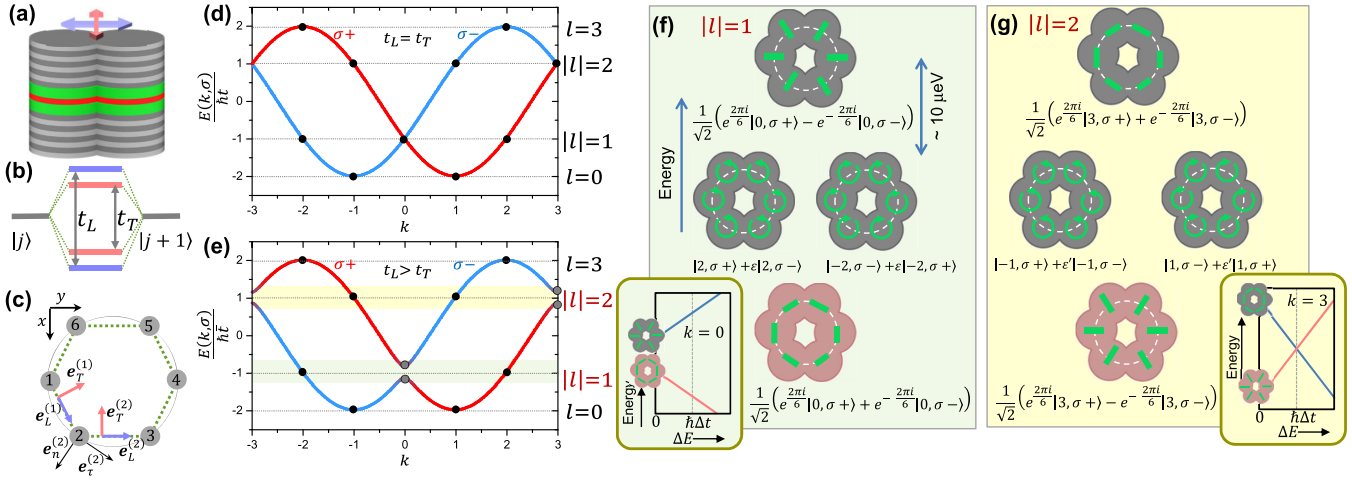

FIG. 2. Spin-orbit split states. (a) Scheme of two coupled pillars showing different tunneling probabilities for photons polarized longitudinal (light blue) and transverse (pink) to the link. (b) This results in polarization splitting of the bonding and antibonding states. (c) Scheme of the unit vectors longitudinal and transverse to each link, and radial and azimuthal on each site, used to calculate the SO-coupled eigenstates of Hamiltonian (3). (d) Polarization-dependent classification of the energy states in the absence of SO coupling ($t_L = t_T$ and $\Delta E = 0$) as a function of their total momentum $k = l + \sigma$. States located on each horizontal line have a well-defined orbital momentum l and form degenerate multiplets. (e) Same as (d) for $t_L \gtrsim t_T$. The SO coupling is evidenced in the anticrossing of the bands, at $k = 0$ and $k = 3$. (f)–(g) Fine structure and polarization pattern of the molecular eigenstates corresponding to the multiplets $l = 1$ (f) and $l = 2$ (g), split by the SO coupling for $\hbar\Delta t > \Delta E$. Note that $\epsilon, \epsilon' \ll 1$ (see Sec. I of Ref. [32]). The salmon color shows the states in which condensation takes place in Figs. 4 and 5. The insets in (f) and (g) show the relative energy of the top and bottom states of each multiplet when $\Delta E > 0$.

III. LOW POWER: SPIN-INDEPENDENT REGIME

The considered hexagonal structure can be described in a tight-binding formalism. If we neglect, for the moment, polarization effects, the Hamiltonian describing the tunneling of polaritons from pillar to pillar reads

$$H = -\sum_{j=1}^{6} \hbar t(\hat{a}_{j+1}^{\dagger} \cdot \hat{a}_j + \hat{a}_j^{\dagger} \cdot \hat{a}_{j+1}), \tag{1}$$

where the $\hat{a}_j$ operator destroys a polariton in site $j = 1, \ldots, 6$ and t is the tunneling probability. This Hamiltonian is analogous to that describing the tunneling between electronic p_z states of the C_6H_6 benzene molecule. The eigenfunctions are delocalized over the whole structure, with a lobe centered on each micropillar. They can be classified in terms of the orbital angular momentum $l = 0, \pm 1, \pm 2, 3$, which determines the relative phase between lobes in different micropillars [Fig. 1(c)]:

$$\hat{a}_l = \sum_{j=1}^{6} \frac{1}{\sqrt{6}} e^{i2\pi lj/6} \hat{a}_j. \tag{2}$$

The wave function of the $l = 0$ state presents a constant phase over all the pillars, while the $l = \pm 1, \pm 2$ states contain phase vortices of topological charge l (the phase changes by $2\pi l$ when going around the molecule). Finally, the $l = 3$ state presents a phase change of π from pillar to pillar. The eigenenergies depend on l as follows: $E(l) = E(|l|) = -2\hbar t \cos(2\pi l/6)$, resulting in four energy levels as sketched in Fig. 1(c).

In order to probe the energy spectrum and eigenfunctions of the hexagonal molecule, we perform photoluminescence experiments at 10 K. The sample is excited out of resonance with a Ti:Sapph continuous wave laser, focused on a 12-μm-diameter spot, entirely covering a single molecule. The energy-resolved photoluminescence is recorded by a CCD camera.

Figure 1(b) shows the energy-resolved emission, without any polarization selection, from the lowest four energy levels of the molecule at low excitation density, in the spontaneous emission regime. The measured polariton linewidth is 90 μeV, greater than that expected from the measured Q factor in a resonant transmission experiment (45 μeV at the considered detuning). This widening could be caused by the spectral wandering of the emission line in photoluminescence experiments due to fluctuations in the charge environment of the quantum wells. As the measured linewidth is much larger than the expected difference in tunneling energies for different polarizations (10–20 μeV [31]), the spontaneous emission is effectively unpolarized. This situation is well described by Hamiltonian (1): The four energy levels shown in Fig. 1(b) arise from the coupling of the lowest energy mode of each micropillar. In order to evidence the intensity and phase structure of the eigenfunctions, we perform an energy-resolved tomographic analysis of the emission, following the method used in Ref. [34]. Figure 1(d) shows the spatial distribution

of the total intensity emitted by each level, with maxima located at the center of each micropillar, as expected from the tight-binding calculation, Eq. (2).

The phase structure of the eigenmodes can be accessed by performing interferometric measurements in the following way [35]. The photoluminescence from the ensemble of the molecule is made to interfere with a magnified image of the emission from one of the micropillars [marked with a solid arrow in Fig. 1(d)], which provides a phase reference. Both images are superimposed at the entrance slit of the spectrometer with different angles of incidence, giving rise to interference fringes. In the spectrometer, each emission line is resolved in energy, reaching a different position in a charge coupled device (CCD) camera. Thus, in the CCD, we record the interference between the reference emission and that from the whole molecule for each energy level. The above-mentioned tomographic technique allows us to reconstruct the two-dimensional normalized interferogram for each level, as shown in Fig. 1(e). By applying an off-diagonal Fourier-transform analysis, we extract the phase of the emission relative to that of the reference micropillar, as shown in Fig. 1(f).

The nondegenerate ground state, $E(l=0)$, shows the same phase in the center of each micropillar, as can be seen by following the dotted line in the lower panel of Fig. 1(f) (the radial variation of the phase is an artifact arising from the geometry of the interferometric experiment). Level $E(1)$ is doubly degenerate, the emission being a superposition with equal probability of states with $l=+1$ and $l=-1$ (the relative phase changing from 0 to $+2\pi$ and -2π, respectively, when going around the molecule). In the spontaneous emission regime we are considering, the relative phase between the two substates $l=\pm 1$ changes randomly in time. In this situation, maximum visibility in the interference takes place only at the positions of the micropillar used as a reference and of that located opposite to it [dashed arrow in panel $E(1)$ of Figs. 1(d) and 1(e)]. Both of these pillars share instantaneously the same phase structure with an overall change of π, independent of the relative random phase, resulting in a high fringe visibility. Intermediate pillars mix different phases from the $l=\pm 1$ states, resulting in interference patterns with the reference pillar that change in time depending on the relative random phase between the two substates. For this reason, when averaging in time as done in our experiment, the fringe visibility reduces to zero at points of the molecule located $\pm 90^\circ$ from the reference pillar [32]. This is what is observed in Figs. 1(e)–1(f) for $E(1)$.

A similar situation takes place for the level $E(2)$: The emission arises from the random superposition of the $l=+2$ and $l=-2$ states, the phase now winding from 0 to $+4\pi$ and -4π, respectively. In this case, there are four points of maximum constructive interference, corresponding to the positions in which the phases of both the $l=+2$ and $l=-2$ wave functions are shifted by $n\pi$ ($n=1,2,3,4$) with respect to the reference pillar. Regions of low visibility of fringes are now located at $45^\circ + n\cdot 90^\circ$ from the reference. Finally, the $E(l=3)$ state shows a phase jump of π from pillar to pillar [upper panel in Fig. 1(f)]. All of these observations match the phase distribution expected from the eigenfunctions in Eq. (2) and represented schematically in Fig. 1(c).

The orbital structure we have just evidenced in real space gives rise to distinct patterns in momentum space, as shown in Fig. 1(g), obtained by imaging the Fourier plane of the collection microscope objective on the entrance slit of the spectrometer. To confirm this correspondence, we simulated the momentum space emission of each energy level via the direct Fourier transform of the tight-binding model eigenfunctions [Eq. (2)] assuming a Gaussian on-site wave function. The result, shown in Fig. 1(h), is in good agreement with the experiments.

IV. EMERGENCE OF THE SPIN-ORBIT COUPLING

To show the emergence of spin-orbit coupling for polaritons, we need to extend Hamiltonian (1) to include polarization-dependent effects. The system can be modeled along the lines sketched in Figs. 2(a)–2(c). For each link connecting the pillars $j \leftrightarrow j+1$, we can define a pair of (real) unit vectors $\mathbf{e}_L^{(j)}$ and $\mathbf{e}_T^{(j)}$, respectively longitudinal and transverse to the link direction [see Fig. 2(c)]. In the absence of particle-particle interactions, the tight-binding Hamiltonian describing the six coupled pillars reads

$$\begin{aligned} H = -\sum_{j=1}^{6} \{ & \hbar t_L (\hat{\mathbf{a}}_{j+1}^\dagger \cdot \mathbf{e}_L^{(j)})(\mathbf{e}_L^{(j)\dagger} \cdot \hat{\mathbf{a}}_j) + \text{H.c.} \\ & + \hbar t_T (\hat{\mathbf{a}}_{j+1}^\dagger \cdot \mathbf{e}_T^{(j)})(\mathbf{e}_T^{(j)\dagger} \cdot \hat{\mathbf{a}}_j) + \text{H.c.} \\ & + \Delta E [(\hat{\mathbf{a}}_j^\dagger \cdot \mathbf{e}_\tau^{(j)})(\mathbf{e}_\tau^{(j)\dagger} \cdot \hat{\mathbf{a}}_j) - (\hat{\mathbf{a}}_j^\dagger \cdot \mathbf{e}_n^{(j)})(\mathbf{e}_n^{(j)\dagger} \cdot \hat{\mathbf{a}}_j)] \}, \end{aligned} \tag{3}$$

where $\hat{\mathbf{a}}_j = \mathbf{e}_{\sigma_+}\hat{a}_{j,\sigma_+} + \mathbf{e}_{\sigma_-}\hat{a}_{j,\sigma_-}$ is the vector field operator for polaritons and $\mathbf{e}_\tau^{(j)}$ ($\mathbf{e}_n^{(j)}$) is a unit vector in the azimuthal (radial) direction, parallel (orthogonal) to $\mathbf{e}_L^{(j)} + \mathbf{e}_L^{(j-1)}$. For each site $j=1,\ldots,6$ in the ring, the $\hat{a}_{j,\sigma_+(\sigma_-)}$ operators destroy a polariton in the $\sigma_+(\sigma_-)$ circular polarization basis, which is defined with respect to the Cartesian basis as $\mathbf{e}_{\sigma_\pm} = (\mathbf{e}_x \pm i\mathbf{e}_y)/\sqrt{2}$. t_L and t_T are the tunneling amplitudes for photons with linear polarization oriented along and transverse to the link direction, respectively [see Fig. 2(b)]. In our photonic structure, the microscopic origin of the difference between t_L and t_T can be found in the polarization-dependent penetration of the photon field out of the micropillars. The field penetration close to the region where the micropillars merge affects the overlap of the photonic wave functions, resulting in $t_L \neq t_T$. Finally, the

ΔE terms provide an on-site splitting between linearly polarized states oriented azimuthally ($\mathbf{e}_\tau^{(j)}$) and radially ($\mathbf{e}_n^{(j)}$) to the hexagonal ring shape. These terms account for the waveguidelike geometry of the molecule [36]: If instead of a hexagonal chain we had considered a uniform ring guide, these terms would be the dominant contribution to the SO coupling effects. Note that in Hamiltonian (3), the rigid rotation of the unit vectors $\mathbf{e}_L^{(j)}$, $\mathbf{e}_T^{(j)}$ while going around the hexagon will be crucial to describe the SO coupling.

In the general case of $t_L \neq t_T$ and/or $\Delta E \neq 0$, spin and orbital degrees of freedom are coupled. As it happens to electrons in atoms, in the presence of a finite SO coupling, neither the spin σ nor the orbital angular momentum l is a good quantum number: Hamiltonian (3) is not symmetric under separate orbital or spin rotations. Nevertheless, simultaneous spin and orbital rotations remain symmetry elements, and the corresponding conserved quantity is the total angular momentum $k = l + \sigma$, where $\sigma = \pm 1$ for the $\sigma_\pm$ states. The eigenstates are then better labeled in terms of k, which remains a good quantum number. It is then more convenient to rewrite Hamiltonian (3) in the total angular momentum space basis k as [32]

$$\begin{aligned} H(k,\sigma) \cong & -\sum_{k,\sigma} 2\hbar t \cos(2\pi[k-\sigma]/6)\hat{a}^\dagger_{k,\sigma}\hat{a}_{k,\sigma} \\ & -\sum_k \left(\hbar\Delta t \cos\left(\frac{2\pi k}{6}\right) + \Delta E\right) \\ & \times [\hat{b}^\dagger_{k,\sigma_-}\hat{b}_{k,\sigma_+} e^{-4\pi i/6} + \text{H.c.}] \end{aligned} \tag{4}$$

where $\hat{b}_{k,\sigma} = (1/\sqrt{6})\sum_j e^{-2\pi i(k-\sigma)j/6}\hat{a}_{j,\sigma}$ and $t = (t_L + t_T)/2$ in the limit $\Delta t = t_L - t_T \ll t_{L,T}$, corresponding to the experiments reported below. The second and third lines of Eq. (4) contain the SO coupling terms, which directly arise from the polarization-dependent tunneling Δt and on-site splitting ΔE. Note that in this tight-binding approach, k can only take the values $0, \pm 1, \pm 2, 3$. The geometry of the molecule belongs to the C_6 symmetry group. Thus, $k = +3$ and -3 label the same eigenvalue as they have the same value modulo 6.

Figures 2(d) and 2(e) show the dispersion of the eigenstates of Hamiltonian (4) as a function of k for $\Delta E = 0$ and negligible [Fig. 2(d)] or significant [Fig. 2(e)] values of $\Delta t > 0$. As compared to the l-dependent dispersion, the k-dependent dispersions for the two $\sigma_\pm$ spin states are shifted by ± 1 units of total angular momentum. The crossing visible in Fig. 2(d) at $k = 0$ and $k = 3$ for $\Delta t = 0$ and $\Delta E = 0$ is lifted by the mixing of the two spin components by the SO coupling when $\Delta t \neq 0$ and/or $\Delta E \neq 0$ [Fig. 2(e)]. The mixing thus gives rise to a fine structure in the energy spectrum. At $k = 0$ (respectively, $k = 3$), the magnitude of the splitting between the two states is $\Delta E_{\text{SO}} = 2|+\hbar\Delta t + \Delta E|$ (respectively, $\Delta E_{\text{SO}} = 2|-\hbar\Delta t + \Delta E|$).

With respect to the orbital form, the two $k = 0$ eigenstates are symmetric and antisymmetric combinations of states with opposite circular polarization $\sigma_\pm$ (and, therefore, opposite orbital angular momentum $l = \mp 1$):

$$\begin{aligned} |\psi_{\text{upper}}(k=0)\rangle = \frac{1}{\sqrt{2}}(e^{(2\pi i/6)}|k=0(l=-1),\sigma_+\rangle \\ - e^{(-2\pi i/6)}|k=0(l=+1),\sigma_-\rangle), \end{aligned} \tag{5}$$

$$\begin{aligned} |\psi_{\text{lower}}(k=0)\rangle = \frac{1}{\sqrt{2}}(e^{(2\pi i/6)}|k=0(l=-1),\sigma_+\rangle \\ + e^{(-2\pi i/6)}|k=0(l=+1),\sigma_-\rangle). \end{aligned} \tag{6}$$

These particular combinations of spin and orbital phase structures give rise, in real space, to polarization textures oriented in the azimuthal and radial directions, respectively, for the lower and upper states, as represented in Fig. 2(f). The two remaining states of the $|l| = 1$ manifold $|k = -2, \sigma_-\rangle$ and $|k = 2, \sigma_+\rangle$ are well separated in energy from their partners with the same k and opposite spin. They are thus practically unaffected by the SO coupling, and they remain located in between the split-apart states. The marginal mixing with the same k partners is expressed via the coefficient ϵ in Fig. 2(f).

A similar situation takes place at $k = 3$: The resulting eigenstates are symmetric and antisymmetric combinations of orbital states with opposite circular polarization and opposite angular momentum $l = \pm 2$:

$$\begin{aligned} |\psi_{\text{upper}}(k=3)\rangle = \frac{1}{\sqrt{2}}(e^{(2\pi i/6)}|k=3(l=2),\sigma_+\rangle \\ + e^{(-2\pi i/6)}|k=3(l=-2),\sigma_-\rangle), \end{aligned} \tag{7}$$

$$\begin{aligned} |\psi_{\text{lower}}(k=3)\rangle = \frac{1}{\sqrt{2}}(e^{(2\pi i/6)}|k=3(l=2),\sigma_+\rangle \\ - e^{(-2\pi i/6)}|k=3(l=-2),\sigma_-\rangle). \end{aligned} \tag{8}$$

For small ΔE ($< \hbar\Delta t$), the ordering in energy is exchanged with respect to the $k = 0$ doublet, resulting in an azimuthally polarized lower state and a radially polarized upper state [Fig. 2(g)]. As sketched in the inset of Fig. 2(g), for increasing ΔE, the SO splitting can be canceled ($\Delta E = \hbar\Delta t$) or its sign reversed ($\Delta E > \hbar\Delta t$). Note that an alternative description of the SO coupling in terms of an effective magnetic field acting on the pseudospin of the photon is given in Ref. [32], together with the detailed solution of Hamiltonian (3).

Reference [31] points out that the polarization-dependent tunneling term ($\hbar\Delta t$) dominates over the on-site splitting (ΔE), as sketched for the case of two pillars in Fig. 2(b). This result is further confirmed by performing a

two-dimensional finite-elements mode calculation (COMSOL) using Maxwell's equations for the hexagonal geometry of our structure in the infinite guide approximation [32]. This method has been used in the past to successfully calculate the shape and energy of the eigenmodes in semiconductor micropillars [37]. The simulation shows the same level ordering and polarization patterns as those in Figs. 2(f) and 2(g). By fitting the energy splittings ΔE_{SO} obtained from the mode calculation with the results of the tight-binding model [Eq. (4)], we estimate values of $\hbar\Delta t = 6\ \mu$eV and $\Delta E = 5\ \mu$eV ($\hbar\Delta t > \Delta E$). A more precise estimate of the value of the splittings would require a full three-dimensional finite-elements simulation to account for the polarization-dependent penetration of the electromagnetic field in the vertically confining Bragg mirrors. This mechanism would provide an additional momentum-dependent splitting and should be more important for higher energy states (i.e., the multiplet $|l| = 2$). In planar microcavities, this mechanism is responsible for the so-called optical spin-Hall effect for polaritons and photons propagating at high speeds [9,38]. In our analysis, we neglected this contribution since it does not seem to play a major role in the coupling of the ground state of the micropillars, as reported in previous experiments with two coupled micropillars [31].

In our experimental configuration, the smoking gun for the presence of the spin-orbit coupling described by Hamiltonian (4) would be the observation of eigenstates with the radial or azimuthal polarization patterns sketched in Figs. 2(f) and 2(g). This is the goal of the experiments presented below. As the broad linewidth of the emission under a weak incoherent pump does not allow resolving the spin-orbit split states, in the next section we study the emission under a stronger pump: Polariton condensation occurs [39] and the emission linewidth is dramatically reduced.

V. HIGH-POWER EXPERIMENTS

The polarization patterns associated with the spin-orbit coupled states depicted in Figs. 2(f) and 2(g) can be evidenced at high excitation density, when polariton condensation takes place and the population ends up accumulating in a single quantum state with a reduced linewidth [39]. As usual in nonequilibrium systems, condensation does not necessarily occur in the ground state, and the steady state is determined by the nonlinear interplay between pumping, relaxation, and decay [40–43]. A key element in the selection of the condensed state is the spatial overlap between the incoherent reservoir that feeds the condensate, and the wave functions. The spatial profile of the reservoir is strongly affected by the relaxation into the condensate, while the shape of the latter can be significantly modified because of polariton-polariton interactions [29,32].

In our structure, we observe two nonlinear thresholds in the emission intensity as a function of pumping, corresponding to condensation in two different states. Figure 3 shows the emitted spectrum in momentum space at different excitation powers. Between 7 and 17 mW [Figs. 3(a) and 3(b)], below the first threshold, incoherent relaxation of carriers populates several low-energy states. When increasing the excitation density, we observe the blueshift of all of them caused by the interaction of polaritons with reservoir excitons. At 25 mW [Fig. 3(c)], condensation takes place in the $E(2)$ level. At higher power, 57 mW [Fig. 3(d)], we observe simultaneous condensation in the $E(1)$ and $E(2)$ levels. Finally, above 84 mW [Figs. 3(e) and 3(f)], only the $E(1)$ level remains highly occupied. Note that the redshift observed for the $E(1)$ level between 57 and 110 mW arises from the heating of the sample due to the large absorbed optical density. The photoluminescence intensity emitted by levels $E(1)$ and $E(2)$ is depicted in Fig. 3(g), showing

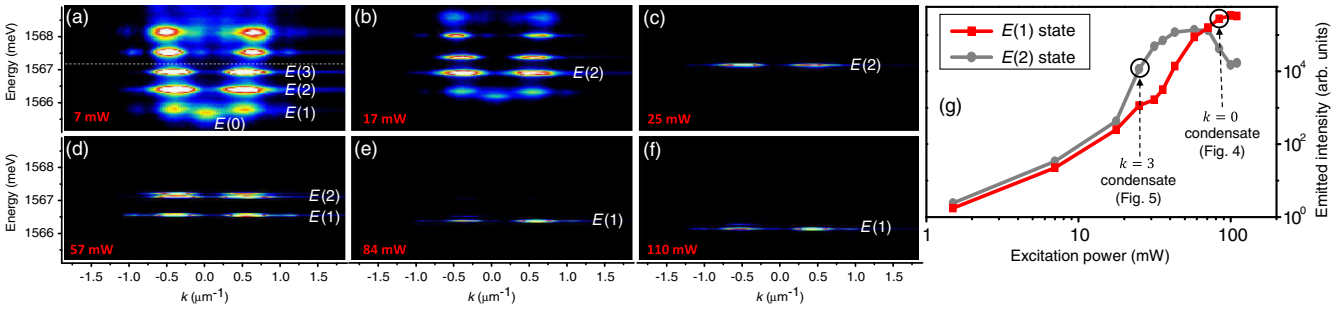

FIG. 3. Power dependence of the condensation process. (a)–(f) Energy- and momentum-resolved emission of the molecule as a function of the excitation power, indicated in each panel. At low power (a), the $E(0), \ldots, E(3)$ energy levels are visible along with higher energy states (above the dashed line) arising from the coupling of higher energy modes of each individual pillar [32]. When increasing the excitation power, polariton condensation occurs first in one of the states of the multiplet $E(2)$ (c) and then in one of the states of the multiplet $E(1)$ (e,f). In (d), the double line in $E(2)$ arises from fluctuations in the position of the pump spot during the measurement (see Sec. E of Ref. [32]). These fluctuations were absent in the experiments shown in Figs. 4 and 5. (g) Emitted intensity of the $E(1)$ and $E(2)$ states as a function of the excitation power. The circles indicate the power at which the experiments shown in Figs. 4 and 5 were performed.

the subsequent condensation in these levels. This condensation dynamics is well described by a semiclassical Boltzmann-equation model, detailed in Ref. [32].

The combination of a reduced linewidth and condensation in excited states grants access to the structure caused by SO coupling in the polaritonic hexagonal molecule. The polarization textures characteristic of the SO split levels can then be monitored by analyzing the six Stokes polarization components: linear vertical, horizontal, diagonal, antidiagonal, and circular σ_+ and σ_- [32]. In the case shown in Fig. 4 (excitation intensity of 84 mW), polaritons condense in the lowest state arising from the $|l| = 1$ quadruplet, that is, into the lowest state at $k = 0$ [Fig. 2(f)]. This fact is evidenced when mapping the linear polarization of the emission [Fig. 4(g)]: The polarization is directed in the azimuthal direction around the molecule as predicted in Fig. 2(f) and described in Eq. (6). The polarization-selective interferometric analysis of the emission in the circular basis shown in Figs. 4(c)–4(f) reveals the underlying helical orbital structure of the state, consisting of the linear superposition of two states of opposite orbital vorticity $l = \pm 1$ and opposite spins. For each spin state $\sigma_\mp$, the phase winds by $\pm 2\pi$ while looping around the molecule. A detailed Stokes vector analysis of the emission can be found in Ref. [32].

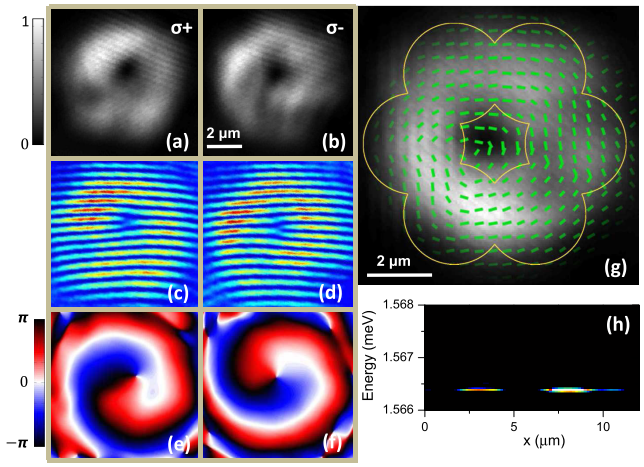

FIG. 4. Condensation in the $k = 0$ state of the $E(1)$ manifold. (a,b) Real space emission in the σ_+ and σ_- circular polarizations for a polariton condensate in the state $|\psi_{\text{lower}}(k = 0)\rangle$, at a pumping intensity of 84 mW. Each polarization component contains a vortical current in the clockwise (σ_+) and counterclockwise (σ_-) directions, evidenced in the forklike dislocations apparent in the interferometric measurements shown in (c) and (d), respectively, and in the extracted phase gradients in (e) and (f). The phase changes from 0 to $\mp 2\pi$ when circumventing the molecule. (g) The green traces show the plane of linear polarization of the emission measured locally, superimposed to the total emitted intensity of the molecule. The condensate shows azimuthal linear polarization. Solid lines depict the contour of the microstructure. (h) Spatially resolved emission spectrum.

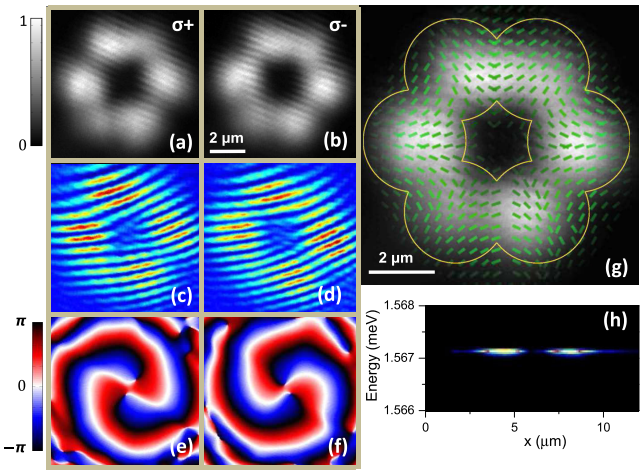

FIG. 5. Condensation in the $k = 3$ state of the $E(2)$ manifold. (a,b) Real space emission in the σ_+ and σ_- circular polarizations for a polariton condensate in the state $|\psi_{\text{lower}}(k = 3)\rangle$, at 25 mW. Each polarization component contains a vortical current of double phase charge in the counterclockwise (σ_+) and clockwise (σ_-) directions, evidenced in the double forklike dislocations apparent in the interferometric measurements shown in (c) and (d), respectively, and in the extracted phase gradients in (e) and (f). The phase changes from 0 to $\pm 4\pi$ when circumventing the molecule. (g) The green traces show the plane of linear polarization of the emission measured locally, superimposed to the total emitted intensity of the molecule. At the center of each micropillar, the condensate shows a linear polarization pattern pointing radially. Solid lines depict the contour of the microstructure. (h) Spatially resolved emission spectrum.

Condensation in other SO-coupled states can be observed by varying the excitation conditions [Fig. 3(g)]. For a 25 mW excitation density, polariton condensation takes place in the lowest energy state of the $|l| = 2$ quadruplet [Fig. 2(g)], with $k = 3$, described by Eq. (8). This situation is shown in Fig. 5. Within the pillars, the emission is linearly polarized along the radial direction [Fig. 5(g)] as predicted for the lowest state of Fig. 2(g). The complete pattern is reproduced by the finite-element calculation corresponding to this level and shown in Fig. S7(b). The polarization-selective interferometric images of Figs. 5(c)–5(f) evidence the underlying orbital structure of the state, consisting in the linear superposition of two states of opposite spin and opposite orbital angular momentum. In contrast to the case of Fig. 4, the extracted phase [Figs. 5(e) and 5(f)] changes from zero to $\pm 4\pi$ while looping around the molecule.

VI. CONCLUSIONS

We have shown the emergence of spin-orbit coupling in a polariton structure made out of coupled micropillars. In our experiments, polariton condensation occurs selectively in two SO-split states holding the polarization textures shown in Figs. 4 and 5. The polarization patterns of the other states

should also be accessible by resorting to a resonant excitation scheme as opposed to the nonresonant one used here. The SO coupling reported here for polaritons originates in the polarization dependence of the photonic confinement and photon tunneling amplitude, which can both be engineered with a suitable design of the structure. For instance, by asymmetrizing the micropillar shape, we can enhance ΔE such that the SO coupling is canceled in the multiplet $|l| = 2$, or its sign reversed, as sketched in the inset of Fig. 2(g). The polarization splittings can be additionally manipulated by modifying the geometry of the layers forming the cavity and Bragg mirrors, as discussed in Ref. [44]. Notice that the same SO-coupling engineering could be implemented for pure photons, either by choosing a larger exciton-photon detuning or processing an empty cavity.

Further promising developments are expected to occur when the SO coupling is scaled up to larger systems such as two-dimensional lattices, where photonic quantum spin-Hall states [23] and spin topological insulators [5,25,26] can be realized. Exciting new features are anticipated in systems with a high degree of phase frustration, like the optically accessible flat bands recently reported in a honeycomb lattice of micropillars [18]. At strong light intensities, our system appears to be an excellent platform to study the effect of SO coupling on nonlinear topological excitations like vortex solitons [45] and nonlinear ring states [46]. When the strong polariton nonlinearities are brought towards the single-particle level, new quantum features are expected to originate while polaritons enter a strongly correlated state [19].

ACKNOWLEDGMENTS

We thank J. W. Fleischer, M. Hafezi, G. Molina-Terriza, A. Poddubny, P. Voisin, and M. Wouters for fruitful discussions. This work was supported by the French RENATECH, the ANR-11-BS10-001 contract QUANDYDE, the ANR-11-LABX-0014 Ganex, the RTRA Triangle de la Physique (contract Boseflow1D), the FP7 ITNs "Clermont4" (235114) and "INDEX" (289968), the FP7 IRSES "Polaphen" (246912), the POLATOM ESF Network, the Nanosaclay Labex, and the ERC grants Honeypol and QGBE.

[1] I. Zutic, J. Fabian, and S. Das Sarma, *Spintronics: Fundamentals and Applications*, Rev. Mod. Phys. **76**, 323 (2004).

[2] Y. K. Kato, R. C. Myers, A. C. Gossard, and D. D. Awschalom, *Observation of the Spin Hall Effect in Semiconductors*, Science **306**, 1910 (2004).

[3] J. Wunderlich, B. Kaestner, J. Sinova, and T. Jungwirth, *Experimental Observation of the Spin-Hall Effect in a Two-Dimensional Spin-Orbit Coupled Semiconductor System*, Phys. Rev. Lett. **94**, 047204 (2005).

[4] J. D. Koralek, C. P. Weber, J. Orenstein, B. A. Bernevig, S.-C. Zhang, S. Mack, and D. D. Awschalom, *Emergence of the Persistent Spin Helix in Semiconductor Quantum Wells*, Nature (London) **458**, 610 (2009).

[5] C. L. Kane and E. J. Mele, *Quantum Spin Hall Effect in Graphene*, Phys. Rev. Lett. **95**, 226801 (2005).

[6] V. Galitski and I. B. Spielman, *Spin-Orbit Coupling in Quantum Gases*, Nature (London) **494**, 49 (2013).

[7] D. N. Christodoulides, F. Lederer, and Y. Silberberg, *Discretizing Light Behaviour in Linear and Nonlinear Waveguide Lattices*, Nature (London) **424**, 817 (2003).

[8] A. Kavokin, G. Malpuech, and M. Glazov, *Optical Spin Hall Effect*, Phys. Rev. Lett. **95**, 136601 (2005).

[9] C. Leyder, M. Romanelli, J. Ph. Karr, E. Giacobino, T. C. H. Liew, M. M. Glazov, A. V. Kavokin, G. Malpuech, and A. Bramati, *Observation of the Optical Spin Hall Effect*, Nat. Phys. **3**, 628 (2007).

[10] X. Yin, Z. Ye, J. Rho, Y. Wang, and X. Zhang, *Photonic Spin Hall Effect at Metasurfaces*, Science **339**, 1405 (2013).

[11] T. Kitagawa, M. A. Broome, A. Fedrizzi, M. S. Rudner, E. Berg, I. Kassal, A. Aspuru-Guzik, E. Demler, and A. G. White, *Observation of Topologically Protected Bound States in Photonic Quantum Walks*, Nat. Commun. **3**, 882 (2012).

[12] M. C. Rechtsman, J. M. Zeuner, Y. Plotnik, Y. Lumer, D. Podolsky, F. Dreisow, S. Nolte, M. Segev, and A. Szameit, *Photonic Floquet Topological Insulators*, Nature (London) **496**, 196 (2013).

[13] M. Hafezi, S. Mittal, J. Fan, A. Migdall, and J. M. Taylor, *Imaging Topological Edge States in Silicon Photonics*, Nat. Photonics **7**, 1001 (2013).

[14] M. Hafezi, E. A. Demler, M. D. Lukin, and J. M. Taylor, *Robust Optical Delay Lines with Topological Protection*, Nat. Phys. **7**, 907 (2011).

[15] A. B. Khanikaev, S. H. Mousavi, W.-K. Tse, M. Kargarian, A. H. MacDonald, and G. Shvets, *Photonic Topological Insulators*, Nat. Mater. **12**, 233 (2013).

[16] N. Y. Kim, K. Kusudo, C. Wu, N. Masumoto, A. Loffler, S. Hofling, N. Kumada, L. Worschech, A. Forchel, and Y. Yamamoto, *Dynamical d-wave Condensation of Exciton-Polaritons in a Two-Dimensional Square-Lattice Potential*, Nat. Phys. **7**, 681 (2011).

[17] E. A. Cerda-Méndez, D. N. Krizhanovskii, K. Biermann, R. Hey, M. S. Skolnick, and P. V. Santos, *Dynamic Exciton-Polariton Macroscopic Coherent Phases in a Tunable Dot Lattice*, Phys. Rev. B **86**, 100301 (2012).

[18] T. Jacqmin, I. Carusotto, I. Sagnes, M. Abbarchi, D. Solnyshkov, G. Malpuech, E. Galopin, A. Lematre, J. Bloch, and A. Amo, *Direct Observation of Dirac Cones and a Flatband in a Honeycomb Lattice for Polaritons*, Phys. Rev. Lett. **112**, 116402 (2014).

[19] I. Carusotto and C. Ciuti, *Quantum Fluids of Light*, Rev. Mod. Phys. **85**, 299 (2013).

[20] R. Hivet, H. Flayac, D. D. Solnyshkov, D. Tanese, T. Boulier, D. Andreoli, E. Giacobino, J. Bloch, A. Bramati, G. Malpuech, and A. Amo, *Half-Solitons in a Polariton Quantum Fluid Behave Like Magnetic Monopoles*, Nat. Phys. **8**, 724 (2012).

[21] F. Manni, K. G. Lagoudakis, T. C. H. Liew, R. André, V. Savona, and B. Deveaud, *Dissociation Dynamics of Singly*

Charged Vortices into Half-Quantum Vortex Pairs, Nat. Commun. **3**, 1309 (2012).

[22] S. Sinha, R. Nath, and L. Santos, *Trapped Two-Dimensional Condensates with Synthetic Spin-Orbit Coupling*, Phys. Rev. Lett. **107**, 270401 (2011).

[23] A. V. Nalitov, G. Malpuech, H. Tercas, and D. Solnyshkov, *Spin-Orbit Coupling and Optical Spin Hall Effect in Photonic Graphene*, Phys. Rev. Lett. **114**, 026803 (2015).

[24] D. G. Angelakis, M. F. Santos, and S. Bose, *Photon-Blockade-Induced Mott Transitions and XY Spin Models in Coupled Cavity Arrays*, Phys. Rev. A **76**, 031805 (2007).

[25] A. V. Nalitov, D. D. Solnyshkov, and G. Malpuech, *Polariton Z Topological Insulator*, arXiv:1409.6564v1 [Phys. Rev. Lett. (to be published)].

[26] C.-E. Bardyn, T. Karzig, G. Refael, and T. C. H. Liew, *Topological Polaritons and Excitons in Garden Variety Systems*, arXiv:1409.8282v2.

[27] R. O. Umucalilar and I. Carusotto, *Fractional Quantum Hall States of Photons in an Array of Dissipative Coupled Cavities*, Phys. Rev. Lett. **108**, 206809 (2012).

[28] R. O. Umucalilar and I. Carusotto, *Many-Body Braiding Phases in a Rotating Strongly Correlated Photon Gas*, Phys. Lett. A **377**, 2074 (2013).

[29] M. Galbiati, L. Ferrier, D. D. Solnyshkov, Dimitrii Tanese, E. Wertz, A. Amo, M. Abbarchi, P. Senellart, I. Sagnes, A. Lemaitre, E. Galopin, G. Malpuech, and J. Bloch, *Polariton Condensation in Photonic Molecules*, Phys. Rev. Lett. **108**, 126403 (2012).

[30] M. Abbarchi, A. Amo, V. G. Sala, D. D. Solnyshkov, H. Flayac, L. Ferrier, I. Sagnes, E. Galopin, A. Lemaitre, G. Malpuech, and J. Bloch, *Macroscopic Quantum Self-Trapping and Josephson Oscillations of Exciton Polaritons*, Nat. Phys. **9**, 275 (2013).

[31] S. M. de Vasconcellos, A. Calvar, A. Dousse, J. Suffczynski, N. Dupuis, A. Lematre, I. Sagnes, J. Bloch, P. Voisin, and P. Senellart, *Spatial, Spectral and Polarization Properties of Coupled Micropillar Cavities*, Appl. Phys. Lett. **99**, 101103 (2011).

[32] See Supplemental Material at http://link.aps.org/supplemental/10.1103/PhysRevX.5.011034 for additional experiments, Maxwell's equations simulations of the eigenmodes, condensation kinetics simulations, and the detailed solution of the spin-orbit Hamiltonian.

[33] D. Bajoni, P. Senellart, E. Wertz, I. Sagnes, A. Miard, A. Lemaitre, and J. Bloch, *Polariton Laser Using Single Micropillar GaAs-GaAlAs Semiconductor Cavities*, Phys. Rev. Lett. **100**, 047401 (2008).

[34] G. Nardin, T. K. Paraïso, R. Cerna, B. Pietka, Y. Léger, O. E. Daif, F. Morier-Genoud, and B. Deveaud-Plédran, *Probability Density Optical Tomography of Confined Quasiparticles in a Semiconductor Microcavity*, Appl. Phys. Lett. **94**, 181103 (2009).

[35] F. Manni, K. G. Lagoudakis, T. C. H. Liew, R. André, and B. Deveaud-Plédran, *Spontaneous Pattern Formation in a Polariton Condensate*, Phys. Rev. Lett. **107**, 106401 (2011).

[36] C. Sturm, D. Tanese, H. S. Nguyen, H. Flayac, E. Galopin, A. Lematre, I. Sagnes, D. Solnyshkov, A. Amo, G. Malpuech, and J. Bloch, *All-Optical Phase Modulation in a Cavity-Polariton Mach-Zehnder Interferometer*, Nat. Commun. **5**, 3278 (2014).

[37] J. M. Gérard, D. Barrier, J. Y. Marzin, R. Kuszelewicz, L. Manin, E. Costard, V. Thierry-Mieg, and T. Rivera, *Quantum Boxes as Active Probes for Photonic Microstructures: The Pillar Microcavity Case*, Appl. Phys. Lett. **69**, 449 (1996).

[38] M. Maragkou, C. E. Richards, T. Ostatnick, A. J. D. Grundy, J. Zajac, M. Hugues, W. Langbein, and P. G. Lagoudakis, *Optical Analogue of the Spin Hall Effect in a Photonic Cavity*, Opt. Lett. **36**, 1095 (2011).

[39] J. Kasprzak, M. Richard, S. Kundermann, A. Baas, P. Jeambrun, J. M. J. Keeling, F. M. Marchetti, M. H. Szymanska, R. Andre, J. L. Staehli, V. Savona, P. B. Littlewood, B. Deveaud, and L. S. Dang, *Bose-Einstein Condensation of Exciton Polaritons*, Nature (London) **443**, 409 (2006).

[40] M. Richard, J. Kasprzak, R. Romestain, R. Andre, and L. S. Dang, *Spontaneous Coherent Phase Transition of Polaritons in CdTe Microcavities*, Phys. Rev. Lett. **94**, 187401 (2005).

[41] M. Wouters, I. Carusotto, and C. Ciuti, *Spatial and Spectral Shape of Inhomogeneous Nonequilibrium Exciton-Polariton Condensates*, Phys. Rev. B **77**, 115340 (2008).

[42] M. Maragkou, A. J. D. Grundy, E. Wertz, A. Lemaitre, I. Sagnes, P. Senellart, J. Bloch, and P. G. Lagoudakis, *Spontaneous Nonground State Polariton Condensation in Pillar Microcavities*, Phys. Rev. B **81**, 081307 (2010).

[43] L. Ge, A. Nersisyan, B. Oztop, and H. E. Tureci, *Pattern Formation and Strong Nonlinear Interactions in Exciton-Polariton Condensates*, arXiv:1311.4847v1.

[44] G. Panzarini, L. C. Andreani, A. Armitage, D. Baxter, M. S. Skolnick, V. N. Astratov, J. S. Roberts, A. V. Kavokin, M. R. Vladimirova, and M. A. Kaliteevski, *Exciton-Light Coupling in Single and Coupled Semiconductor Microcavities: Polariton Dispersion and Polarization Splitting*, Phys. Rev. B **59**, 5082 (1999).

[45] E. A. Ostrovskaya and Y. S. Kivshar, *Matter-Wave Gap Vortices in Optical Lattices*, Phys. Rev. Lett. **93**, 160405 (2004).

[46] V. E. Lobanov, Y. V. Kartashov, V. A. Vysloukh, and L. Torner, *Stable Radially Symmetric and Azimuthally Modulated Vortex Solitons Supported by Localized Gain*, Opt. Lett. **36**, 85 (2011).